

Rational Design of Porous Nodal-Line Semimetallic Carbon for K-Ion Battery Anode Materials

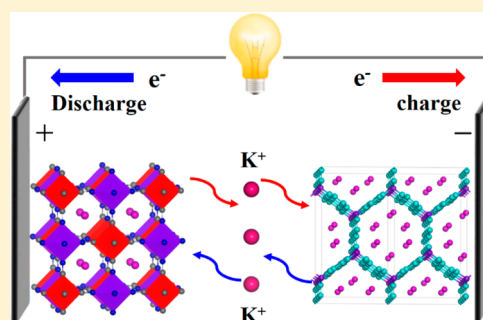
Xiaoyin Li,^{†,||} Jie Liu,^{†,||} Fancy Qian Wang,[†] Qian Wang,^{*,†,||} and P. Jena^{‡,||}

[†]Center for Applied Physics and Technology, Department of Materials Science and Engineering, HEDPS, and BKL-MEMD, College of Engineering, Peking University, Beijing 100871, China

[‡]Department of Physics, Virginia Commonwealth University, Richmond, Virginia 23284, United States

S Supporting Information

ABSTRACT: The potassium-ion battery (KIB), as one of the most promising alternatives to the lithium-ion battery (LIB), has recently received considerable attention. One of the challenges in KIBs is the design and synthesis of high-performance anode materials with high capacity, high rate performance, and good cycling stability. Here, on the basis of first-principles calculations, we propose a three-dimensional (3D) porous nodal-line semimetal carbon allotrope, named BDL-14, consisting of benzene rings incorporated into the diamond lattice, as a potential candidate. With low mass density (1.41 g/cm³), ordered channels, high carrier velocity (0.83 × 10⁶ m/s), high specific capacity (478.23 mAh/g), very low energy barriers (0.05–0.08 eV) for K-ion diffusion, and a small volume expansion (7.03%) during charging and discharging processes, BDL-14 can surpass the properties of anodes currently being considered.



Current lithium-ion battery (LIB) technology cannot meet the ever-growing demand for economical and sustainable battery technologies for advanced electronic devices and vehicles, particularly for large-scale stationary storage. This is primarily because of the limited supply of Li. Consequently, there is an urgent need to develop new battery systems using other elements that are more abundant than Li.^{1–4} To this end, the potassium-ion battery (KIB) system has been considered as one of the most promising candidates because of several unique advantages, such as the exceptionally negative potential of the K⁺/K redox couple (–2.94 V), the relatively high abundance of K resources in the Earth’s crust, and the feasible usage of cheap aluminum (Al) current collector in KIBs because K does not form alloys with Al.^{1,2,5} However, because the size of K is larger than that of Li, the LIB anode materials usually do not work for KIBs. Therefore, it is highly desirable to search for new KIB anode materials with high specific capacity and cycling stability.

Among various candidates, 3D porous semimetallic carbon materials are of special interest.^{6–10} Although numerous 3D porous carbon materials have been extensively studied both theoretically and experimentally,^{11,12} the semimetallic ones with unique electronic band structure appear more intriguing because they mostly possess high electronic conductivity like graphene. Due to their intrinsic porosity, ordered channels, and high electronic conductivity, these materials show great promise for battery applications. To the best of our knowledge, no studies have been reported to date for using the 3D semimetallic carbon allotropes for KIB anodes. In this work, we propose such a material that is constructed by inserting

benzene rings into the well-known diamond lattice. We name this 3D carbon allotrope BDL-14 (Benzene rings incorporated into a Diamond Lattice having 14 atoms per primitive cell). The benzene rings would yield high electronic conductivity because of their aromatic property, while the diamond lattice would result in high structural stability.¹³ Systematic first-principles calculations indeed prove this expectation, demonstrating that BDL-14 possesses intrinsic ordered nanopores for K-ion storage, high electronic conductivity, well-organized channels for fast K-ion diffusion, and small volume change during charging and discharging. All of these extraordinary features endow BDL-14 with the potential for a high-performance anode material for KIBs.

Computational Methods. Calculations of the equilibrium structure, stability, and electronic properties of BDL-14 are based on density functional theory (DFT) as implemented in the Vienna Ab initio Simulation Package (VASP).¹⁴ The exchange–correlation functional is treated by using the form of Perdew–Burke–Ernzerhof (PBE) within the generalized gradient approximation.¹⁵ In addition, the Heyd–Scuseria–Ernzerhof (HSE06) hybrid functional¹⁶ is used to improve the accuracy of electronic band structure calculations. The all-electron projector-augmented wave (PAW) method¹⁷ is used to treat the interactions between ion cores and valence electrons with a plane-wave energy cutoff of 600 eV. For geometry optimization, the convergence criteria for the total

Received: August 23, 2019

Accepted: October 1, 2019

Published: October 1, 2019

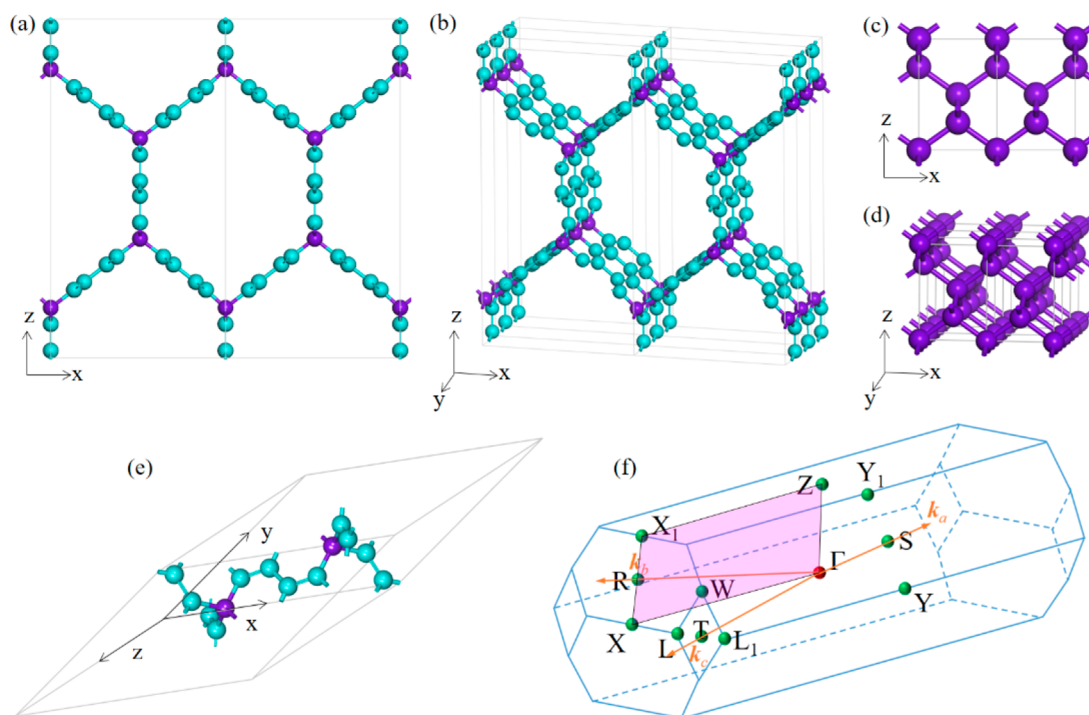


Figure 1. Top and perspective views of (a,b) BDL-14 and (c,d) diamond. (e,f) Primitive cell and corresponding Brillouin zone of BDL-14. The cyan and violet spheres represent sp^2 - and sp^3 -hybridized carbon atoms, respectively.

Table 1. Calculated Equilibrium Structural Parameters Including Lattice Constants a , b , c , Bond Lengths d_{C-C} , the Density ρ , the Energy Difference Relative to Graphite (ΔE), and the Electronic Band Gap E_g at the HSE06 Level for BDL-14, Graphite, Diamond, T6, bct- C_4 , IGN, bco- C_{16} , and Hex- C_{18}

structure	a , b , c (Å)	d_{C-C} (Å)	ρ (g/cm ³)	ΔE (eV)	E_g (eV)
BDL-14	8.94, 2.48, 17.89	1.36–1.49	1.41	0.20	semimetallic
graphite	2.46, 2.46, 7.32	1.42	2.24	0.00	semimetallic
diamond	3.57, 3.57, 3.57	1.55	3.50	0.12	5.36
T6	2.60, 2.60, 6.00	1.34, 1.54	3.06	0.57	metallic
bct- C_4	4.38, 4.38, 2.51	1.52, 1.57	3.42	0.32	3.42
IGN	4.33, 4.33, 2.47	1.41–1.53	2.59	0.23	semimetallic
bco- C_{16}	7.80, 4.90, 3.26	1.38–1.46	2.57	0.39	semimetallic
Hex- C_{18}	8.36, 8.36, 2.46	1.41–1.54	2.41	0.25	metallic

energy and force are set to 10^{-4} eV and 10^{-3} eV/Å, respectively, while for phonon-related calculations, the convergence criteria are improved to 10^{-8} eV and 10^{-6} eV/Å for the total energy and force, respectively. Monkhorst–Pack k -meshes¹⁸ with a grid density of $2\pi \times 0.02 \text{ \AA}^{-1}$ are used for sampling the first Brillouin zone. The thermal stability is studied using ab initio molecular dynamics (AIMD) simulations, where the canonical ensemble (NVT) is employed and temperature control is achieved with the Nosé thermostat.¹⁹ Phonon spectra are calculated by using the finite displacement method as implemented in the Phonopy code.²⁰ The surface spectrum is calculated based on the iterative Green's function method²¹ as implemented in the Wannier Tools package.²² The nudged elastic band (NEB) method²³ is applied to obtain the diffusion energy barrier profiles of potassium ions. The semiempirical long-range dispersion correction (the PBE-D2 functional)²⁴ is used to take into account the effect of van der Waals interactions on the adsorption and migration of K ions.

Geometric Structure and Stability. The optimized structure of the proposed carbon allotrope is shown in Figure 1a,b, which is

constructed by incorporating benzene rings into the diamond lattice, having 14 carbon atoms in its primitive cell, as shown in Figure 1e. The lattice symmetry of BDL-14 is $Im\bar{m}a$ (D_{2h}^{28}), and the calculated equilibrium lattice parameters of its unit cell are $a = 8.94 \text{ \AA}$, $b = 2.48 \text{ \AA}$, and $c = 17.89 \text{ \AA}$. In this structure, there are five nonequivalent crystallographic sites occupying $8i_1$ (0.13, 0.75, 0.20), $8i_2$ (0.19, 0.25, 0.22), $4e_1$ (0.0, 0.25, 0.02), $4e_2$ (0.0, 0.25, 0.10), and $4e_3$ (0.0, 0.75, 0.15) Wyckoff positions, respectively. Its Brillouin zone with high symmetry points is plotted in Figure 1f, which is very complicated. From Figure 1a,b, we note that there are large one-dimensional (1D) channels along the y direction, showing the porous nature of BDL-14, which is desirable for the accommodation and diffusion of K ions. In addition, compared to graphite and diamond, BDL-14 has a much lower density (1.41 g/cm³) because of its intrinsic porosity. For comparison, the equilibrium densities of some other 3D carbon allotropes are also calculated and summarized in Table 1. One can see that BDL-14 has the lowest equilibrium density among those 3D carbon allotropes.

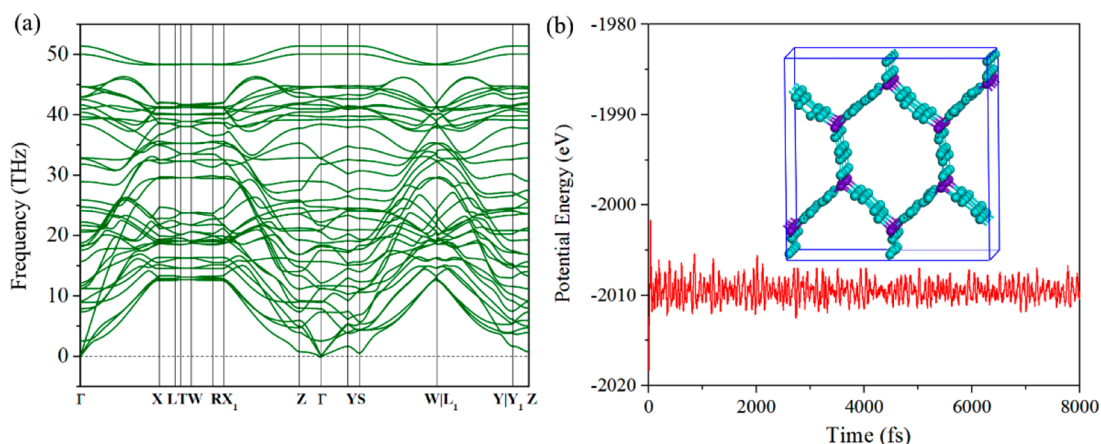


Figure 2. (a) Phonon band structure and (b) total potential energy fluctuation during AIMD simulations of BDL-14 at 300 K. The inset shows the atomic configuration of the $2 \times 4 \times 1$ supercell at the end of AIMD simulations.

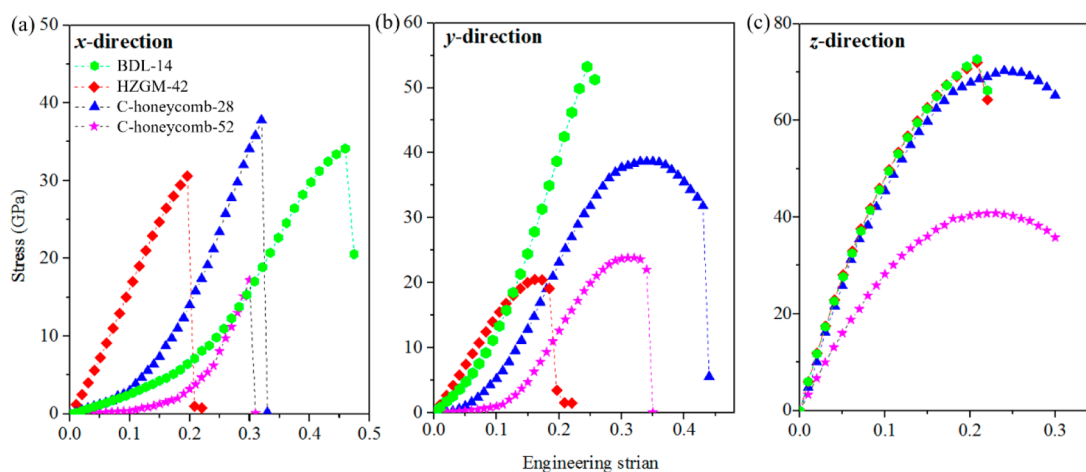


Figure 3. Stress–strain curves for tensile loading along the (a) x , (b) y , and (c) z directions for BDL-14, HZGM-42, C-honeycomb-28, and C-honeycomb-52.

To investigate the energetic stability of BDL-14, we perform total energy calculations and compare them with some other 3D carbon crystals including graphite, diamond, and the recently reported 3D carbon allotropes, such as T6,^{25–28} bct-C₄,²⁹ IGn,³⁰ bco-C₁₆,³¹ and Hex-C₁₈.³² The calculated energy differences (ΔE) with respect to graphite are presented in Table 1, which shows that, although BDL-14 is energetically metastable compared to graphite and diamond, it is more stable than most of the other 3D metastable carbon phases. We further study the bonding feature of this structure to illustrate the origin of its high energetic stability. The calculated bond lengths between the sp^2 -hybridized C atoms are in the range of 1.36–1.48 Å, while the bond length between the sp^3 -hybridized C atoms is 1.49 Å. The bond angles of the sp^2 -hybridized carbon atoms are in the range of 117.1–123.8°, and those of the sp^3 -hybridized carbon atoms are in the range of 109.2–112.4°. As compared to the bond length and bond angle of the sp^2 - and sp^3 -hybridized carbon atoms in graphite (1.42 Å, 120°) and diamond (1.53 Å, 109.5°), the corresponding values of BDL-14 are very close to those ideal values, thus leading to its relatively high energetic stability.

The dynamical stability of BDL-14 is examined by calculating its phonon band structure. As shown in Figure 2a, all vibrational modes in the entire Brillouin zone are real, confirming the dynamical stability of this structure. To study

the thermal stability at room temperature, we perform AIMD simulations at 300 K with a large supercell of $2 \times 4 \times 1$ (see Figure 2b). We find that the skeleton of this structure remains almost intact after heating for 8 ps with a time step of 1 fs, and the total potential energy fluctuates around a constant magnitude during the entire simulation, confirming that BDL-14 is thermally stable at room temperature. In addition, we calculate the elastic constants to verify its mechanical stability (see Table S1). The linear elastic constants of a mechanically stable 3D orthorhombic crystal structure have to satisfy the Born–Huang criteria: $C_{ii} > 0$ ($i = 1, 2, 3, 4, 5, 6$), $[C_{11} + C_{22} + C_{33} + 2(C_{12} + C_{13} + C_{23})] > 0$, $C_{11} + C_{22} - 2C_{12} > 0$, $C_{11} + C_{33} - 2C_{13} > 0$, $C_{22} + C_{33} - 2C_{23} > 0$, $C_{22} + C_{33} - 2C_{23} > 0$.³³ The elastic constants of BDL-14 obey all of the criteria listed above, confirming that this new structure is mechanically stable. It is encouraging to note that benzene molecules can serve as precursors for growing a variety of carbon structures,³⁴ and many 3D porous carbon materials have been experimentally synthesized by assembling carbon nanostructures.^{12,35} In particular, the theoretically predicted T-carbon constructed by geometrical expansion of the diamond lattice with C₄ tetrahedra³⁶ was successfully synthesized by compressing multiwall carbon nanotubes.³⁷ These advances in synthesizing new carbon materials make it very promising for

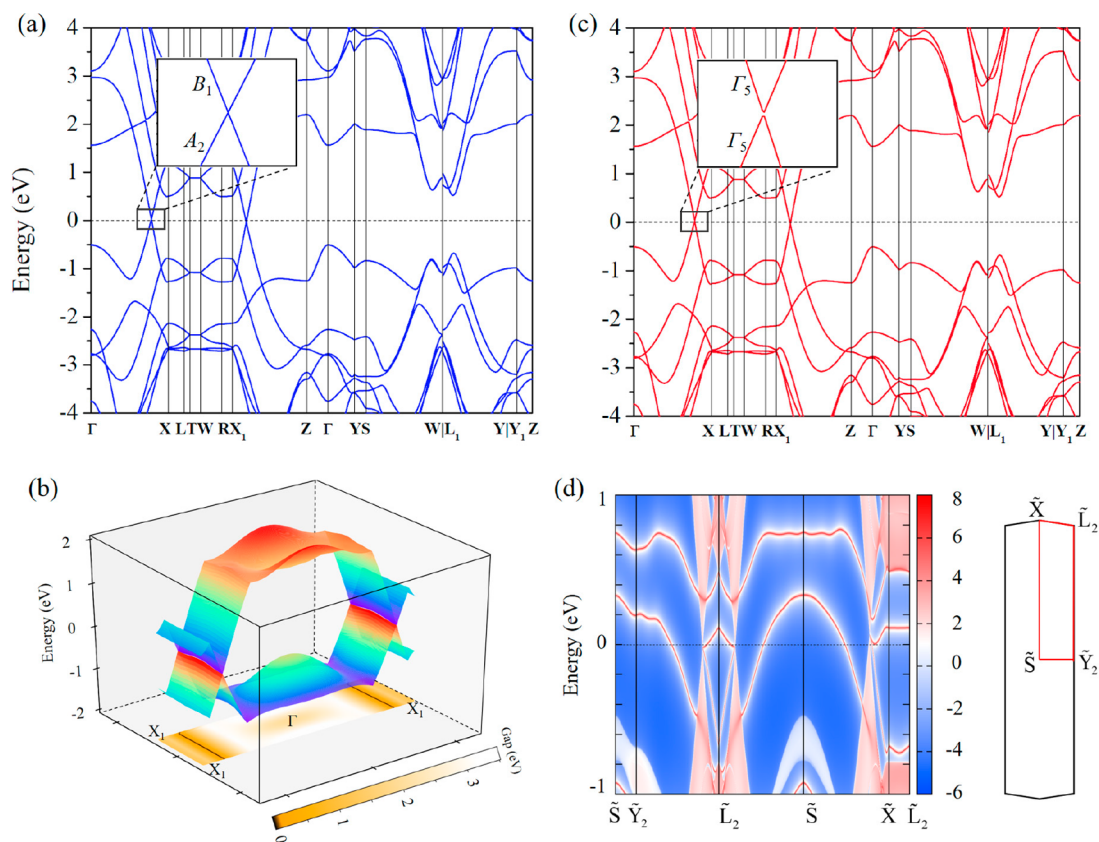


Figure 4. Band structure without (a) and with SOC (c) of BDL-14. (b) 3D (k_1, k_2, energy) band structure and nodal lines of BDL-14 in the Γ - X - Z k plane. The color bar indicates the energy gap between the conduction band and valence band at each k point. (d) Projected surface states and surface Brillouin zone for the (001) surface of BDL-14. Low, medium, and high densities of states are represented by blue, white, and red colors, respectively.

the synthesis of the energetically more stable BDL-14 in the future.

Mechanical Properties. On the basis of the calculated elastic constants of BDL-14, we can derive its Young's moduli along different axial directions. Here, we should point out that, for convenience of comparison, in the calculations related to the mechanical properties we exchange the spatial axis y with z of this structure to make its 1D channels extend along the z direction. The Young's moduli of BDL-14 along the x , y , and z directions are calculated to be 15.30, 45.50, and 625.00 GPa, respectively, showing a highly anisotropic mechanical strength with the Young's modulus along the z direction much larger than that along the x and y directions, which stems from its unique atomic configuration. Compared with some recently reported 3D porous carbon allotropes with a high Young's modulus along the z direction, such as HZGM-42 (612.10 GPa),⁹ C-honeycomb-28 (571.9 GPa),³⁸ and C-honeycomb-52 (353.90),³⁸ BDL-14 possesses the largest Young's modulus, suggesting its stronger specific strength along the z direction.

The mechanical properties are further investigated by calculating its stress-strain curves along different axial directions. The results are displayed in Figure 3. The deformation with a small strain increment of 0.01 is adopted to achieve the quasi-static displacement-controlled deformation. One can see that the fracture strain of BDL-14 under the uniaxial load condition is 0.46, 0.24, and 0.21 along the x , y , and z directions, respectively, suggesting that the proposed structure is able to maintain its structural stability within a wide strain range. We also find that BDL-14 has an ideal tensile

strength (the maximum stress required for breaking the crystal structure)³⁹ of 34.1, 53.3, and 72.7 GPa along the x , y , and z directions, respectively. The ideal tensile strength of BDL-14 along the z direction is higher than that of HZGM-42 (71.9 GPa), C-honeycomb-28 (70.3 GPa), and C-honeycomb-52 (40.1 GPa), confirming its superior load-bearing capacity along this direction. The direction-dependent large Young's modulus and ideal tensile strength of this structure can be explained by the formation of graphene nanoribbons along the z direction, which inherit the high in-plane strength of graphene.

Electronic Properties. To study the electronic properties of BDL-14, we first calculate its band structure using the PBE functional without considering the spin-orbit coupling (SOC). As shown in Figure 4a, along the Γ - X and X_1 - Z paths of the Brillouin zone, the valence and conduction bands of BDL-14 meet at a single point at the Fermi level, forming a Dirac point similar to that of graphene. This suggests that BDL-14 is semimetallic. The band symmetry analysis shows that the crossing bands belong to two different irreducible representations, labeled B_1 and A_2 in Figure 4a, respectively, confirming the unavoidable band crossing in BDL-14. To validate the results calculated at the PBE functional level, we recalculate the band structure by using the more accurate hybrid functional HSE06.¹⁶ The results in Figure S1 show that the band structure shows semimetallic characteristic at the HSE06 level as well, indicating that the semimetallicity is an intrinsic property of this structure. By thoroughly scanning the whole Brillouin zone of BDL-14 (see Figure S2), we find that the crossing points of the valence and conduction bands only

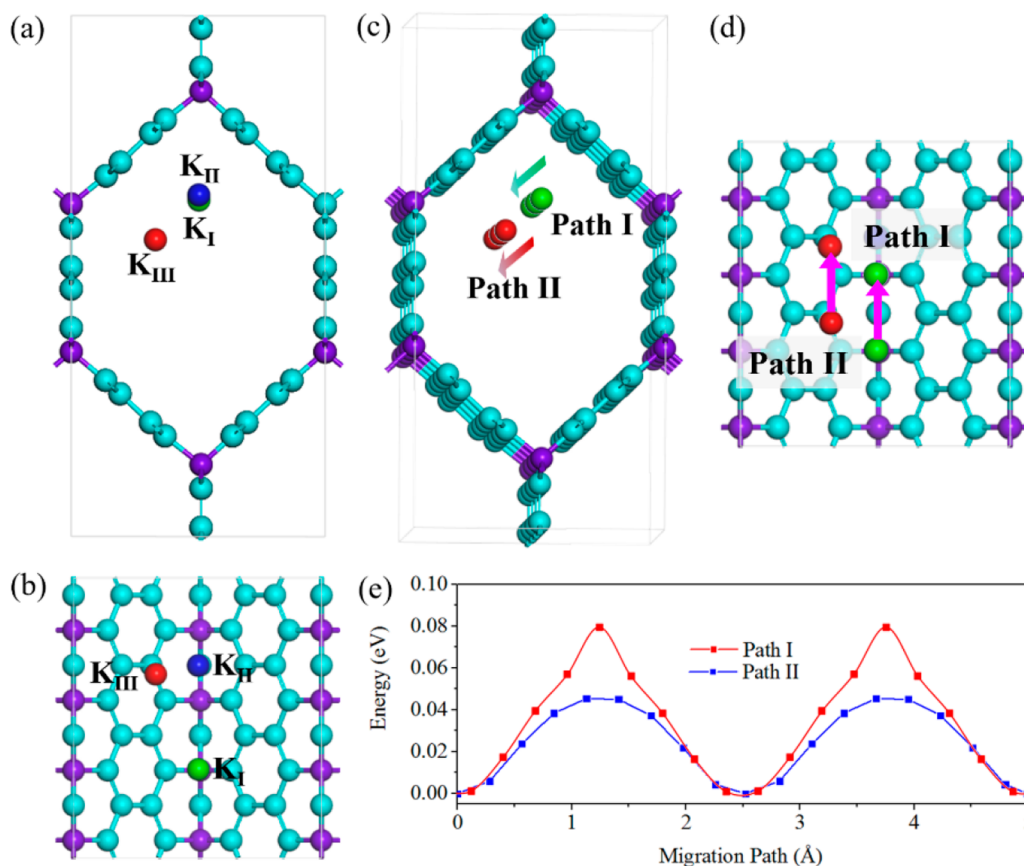


Figure 5. (a,b) Top and side views of possible K absorption sites in BDL-14. (c,d) Two possible migration paths of K ions and (e) corresponding diffusion energy barrier profiles.

exist in the Γ -X-Z k plane (highlighted in Figure 1f). A further analysis of the 3D valence and conduction bands of this k plane (Figure 4b) shows that the crossing points form continuous nodal lines, demonstrating that BDL-14 is a nodal-line semimetal. A detailed analysis of the partial density of states (DOS) projected onto the sp^2 - and sp^3 -hybridized carbon atoms and the band-decomposed charge density near the Fermi energy (Figure S3) demonstrate that the valence and conduction bands primarily originate from the sp^2 -hybridized carbon atoms.

We next investigate the electronic structures of BDL-14 by taking into account SOC. The calculated results are plotted in Figure 4c, showing that a small gap less than 1 meV opens up at the crossing point when considering SOC. This can be understood from the band symmetry analysis. In the presence of SOC, the double point group symmetry should be considered. Thus, the valence and conduction bands belong to the same irreducible representation Γ_5 , which means that the two states can interact with each other, resulting in band opening. By calculating the parity of the wave function of the occupied states at the time-reversal invariant momenta (TRIM), we obtain the Z_2 index of BDL-14 as (0:111), showing that BDL-14 is a 3D weak topological insulator (TI). To confirm the result, we calculate the (001) surface states of BDL-14 with a 30 layer thick slab model. The emerging gapless surface states as presented in Figure 4d agree well with the result of Z_2 index calculation. Although BDL-14 is strictly a weak TI, we can still treat it as a nodal-line semimetal because of the tiny SOC gap (smaller than 1 meV).

In addition, we note that the valence and conduction bands of BDL-14 along the Γ -X direction have linear dispersion similar to that of graphene, implying a possible high carrier velocity along this direction. We then estimate the corresponding carrier velocity using the following formula

$$\vec{v}_{\vec{k}} = \hbar \frac{d\vec{\varepsilon}_{\vec{k}}}{dk} \quad (1)$$

where \hbar is the Planck constant, $\varepsilon_{\vec{k}}$ is the energy, and \vec{k} is the wave vector. To verify the reliability of the method used, we first calculate the carrier velocity of graphene, yielding a result of 0.87×10^6 m/s, very close to the value of 0.86×10^6 m/s reported by Bu et al.⁴⁰ Following the same procedure, the maximum carrier velocity of BDL-14 is calculated to be 0.83×10^6 m/s, which is comparable to that of graphene, showing a good potential of BDL-14 for applications in high-speed electronic devices. More importantly, the relatively high carrier velocity endows BDL-14 with rapid electron transfer capability, which is crucial to improve the rate performance of the anodes. Therefore, the nodal-line semimetal BDL-14 with the porous geometry, 1D channels, and high carrier velocity has the potential as a high-performance anode material for KIBs.

Application as an Anode Material for KIBs. We first examine the adsorption and diffusion of a single K ion in BDL-14 to evaluate the performance of this material as an anode at low K concentration. A $1 \times 4 \times 1$ supercell is used to avoid the interaction between the neighboring K ions. On the basis of the geometric configuration and symmetry of BDL-14, we find three possible initial adsorption sites marked as K_I , K_{II} , and

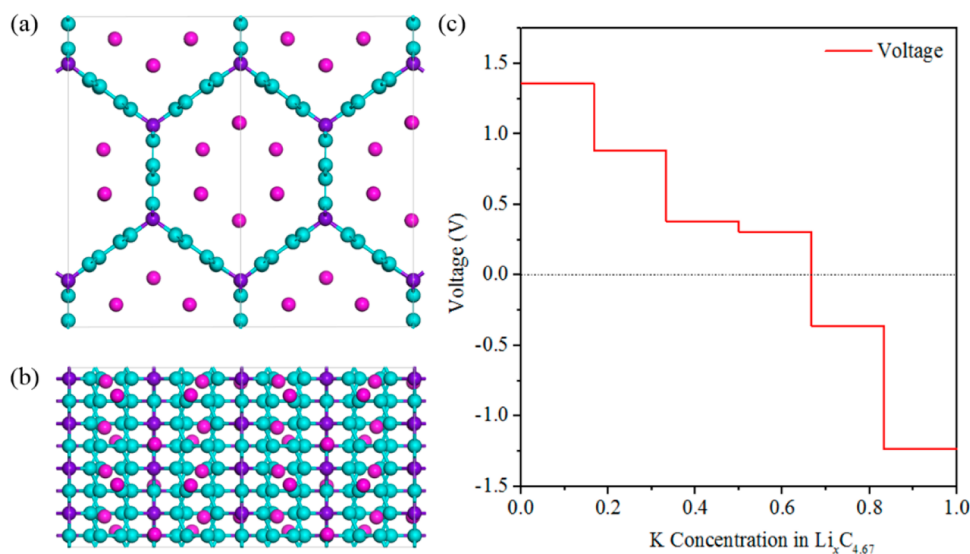


Figure 6. (a) Top and (b) side views of the full K-intercalated configuration of BDL-14. (c) Calculated voltage profile of BDL-14 in the half-cell.

K_{III} , as shown in Figure 5a,b. The K adsorption energy (E_a) is calculated using the following equation

$$E_a = (E_{K_x\text{-BDL-14}} - E_{\text{BDL-14}} - xE_K)/x \quad (2)$$

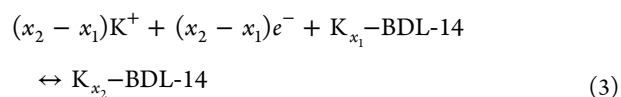
where $E_{K_x\text{-BDL-14}}$ and $E_{\text{BDL-14}}$ are the total energy of K-inserted and pristine BDL-14, respectively. E_K is the energy of one K atom in the bulk metallic phase. After full structural relaxation, K_{II} is optimized to K_{I} , and K_{I} and K_{III} are found to be stable adsorption sites with adsorption energies of -1.64 and -1.33 eV, respectively, indicating strong ionic bonding between K and BDL-14. On the basis of Bader charge population analysis,⁴¹ we find that the K atom adsorbed on the K_{I} and K_{III} sites transfers 0.89 and 0.91 electrons to BDL-14, respectively, indicating that K atoms donate almost all of their valence electrons to BDL-14 and become K ions.

To study the diffusion behavior of K ions in BDL-14, we select two possible diffusion pathways (path I and path II) along the 1D channels, as shown in Figure 5c,d, because K ions in BDL-14 are restricted to the 1D channels. Path I corresponds to the K ion adsorbed on the K_{I} site migrating to its neighboring K_{I} site along the channel, and path II shows that the K ion adsorbed on the K_{III} site migrates to its neighboring K_{III} site along the channel. The calculated diffusion energy barrier profiles are presented in Figure 5e. For both paths I and II, the diffusion barriers are extremely low, namely, 0.081 and 0.045 eV, respectively, which are much lower than that of the K ion in graphite calculated using the same method (0.11–1.58 eV⁴²). This suggests that the mobility of K ions in BDL-14 can be very fast. The ultralow diffusion barriers of K ions in BDL-14 can be attributed to the flat energy landscape along the ordered 1D channel and the large channel size, which is reminiscent of the low diffusion barrier of Li ions in IGN with the 1D ordered channels for Li ion diffusion.⁷

Next, we study the theoretical capacity of BDL-14. We gradually increase the K concentration until the full K-intercalated configuration (see Figure 6a,b) is reached. In this configuration, both stable adsorption sites K_{I} and K_{III} are uniformly distributed, and only half of them are occupied. The average adsorption energy of K in BDL-14 is calculated to be -0.39 eV, suggesting that K atoms can be stably adsorbed and

clustering of K ions will not occur even at such a high concentration. Thus, the theoretical specific capacity of BDL-14 is calculated to be 478.23 mAh/g ($KC_{4.67}$), which is much larger than that of most reported KIB anodes such as graphite (279 mAh/g) and TiO_2 polymorphs (97–308 mAh/g).^{43–45}

We further evaluate the performance of BDL-14 as a KIB anode by calculating its open-circuit voltage (OCV) in the half-cell reaction, described as



Neglecting the effects of volume, pressure, and entropy, the average voltage of $K_x\text{-BDL-14}$ in the concentration range of $x_1 < x < x_2$ can be obtained from the equation⁴⁶

$$V \approx \frac{E_{K_{x_1}\text{-BDL-14}} - E_{K_{x_2}\text{-BDL-14}} + (x_2 - x_1)E_K}{(x_2 - x_1)} \quad (4)$$

where $E_{K_{x_1}\text{-BDL-14}}$, $E_{K_{x_2}\text{-BDL-14}}$, and E_K are the total energies of $K_{x_1}\text{-BDL-14}$, $K_{x_2}\text{-BDL-14}$, and one K atom in the K bulk phase, respectively. To obtain $E_{K_x\text{-BDL-14}}$ at a certain K concentration ($K_xC_{4.67}$: $x = 0.167, 0.333, 0.500, 0.667, 0.833$), we calculate the total energy of 10 different inequivalent adsorption configurations for each concentration and select the one with the lowest adsorption energy (see Figure S4) as $E_{K_x\text{-BDL-14}}$. The voltage profile obtained based on eq 4 is displayed in Figure 6c, which shows three prominent voltage regions ($0 < x < 0.17$, $0.17 < x < 0.33$, and $0.33 < x < 0.67$) corresponding to the weak, increased, and strong repulsive interactions between the K ions at low, medium, and high K concentrations, respectively. One can see that when the K concentration increases to 0.667 the voltage profile decreases to -0.362 V, suggesting that the reversible capacity of BDL-14 in the half-cell is 318.67 mAh/g (KC_7), which is higher than the theoretical specific capacity of graphite (279 mAh/g). The average voltage of BDL-14 in the half-cell can be estimated by numerically averaging the profile in the region $0 < x < 0.67$, which is calculated to be 0.59 V. However, in a full-cell, the repulsive interactions between K ions at high K concentrations

can be overcome by applied voltage during charging, leading to a maximum K capacity (478.23 mAh/g; $KC_{4.67}$) with a lower average voltage of 0.22 V.

Cycling stability, which is mainly determined by the volume change of an anode during the potassium adsorption/desorption processes, is another important factor that should be considered to assess the performance of the KIB anode materials. Comparing the structure of the K-intercalated BDL-14 at different K concentrations with that of the pristine BDL-14, we find no bond-breaking and irreversible reactions occurring during the K insertion/deinsertion processes. Moreover, the volume expansion of BDL-14 is calculated to be 7.03%. This is a considerable improvement over the 61% volume change of graphite used as the KIB anode.³ The small volume expansion of BDL-14 can be attributed to its intrinsic nanopores, which provide a relatively large space to accommodate the K-ions. The small volume change for K-ion insertion and the large fracture strain indicate that BDL-14 can exhibit good cycling stability when used as the KIB anode material.

In summary, on the basis of first-principles calculations together with molecular dynamics simulation and topological analysis, we have identified a new 3D porous carbon BDL-14 as a high-performance KIB anode material with the following features: (i) BDL-14 is not only dynamically, thermally, and mechanically stable but also energetically more favorable than most of the previously reported 3D carbon allotropes; (ii) BDL-14 is a nodal-line semimetal with a high carrier velocity (0.83×10^6 m/s), and good electrical conductivity; (iii) the intrinsic porosity of BDL-14 provides sufficient adsorption sites for K ions, resulting in a large specific capacity of 478.23 mAh/g; (iv) the diffusion energy barriers of the K-ion along the 1D channels in BDL-14 are extremely low (0.05–0.08 eV), enabling fast K-ion transport dynamics; (v) the volume change of BDL-14 is as low as 7.03%, indicating good cycling stability during charging and discharging. These attributes demonstrate the potential of BDL-14 as a high-performance KIB anode. Moreover, because of the smaller size of Li- and Na-ions, we can optimistically expect that BDL-14 is also promising for Li-ion and Na-ion batteries. We hope that our work will stimulate further theoretical and experimental efforts in developing new 3D topological quantum materials, going beyond the conventional materials for new battery technology.

■ ASSOCIATED CONTENT

Supporting Information

The Supporting Information is available free of charge on the ACS Publications website at DOI: 10.1021/acs.jpcl.9b02484.

Additional data and figures including elastic constants for BDL-14 and for other 3D porous carbon allotropes; electronic band structure of BDL-14 at the HSE06 level; electronic band structure of BDL-14 along several highly symmetric paths of the Brillouin zone; partial DOS and band decomposed charge density isosurface of BDL-14; K binding energies of 50 configurations for 5 different K concentrations (PDF)

■ AUTHOR INFORMATION

Corresponding Author

*E-mail: qianwang2@pku.edu.cn.

ORCID

Qian Wang: 0000-0002-9766-4617

P. Jena: 0000-0002-2316-859X

Author Contributions

†X.L. and J.L. contributed equally to this work.

Notes

The authors declare no competing financial interest.

■ ACKNOWLEDGMENTS

This work is partially supported by grants from the National Natural Science Foundation of China (Grants No. 21773004, No. 11974028), the National Key Research and Development Program of China (2016YFE0127300, 2017YFA0205003), and is supported by the High Performance Computing Platform of Peking University, China. P.J. acknowledges support by the U.S. Department of Energy, Office of Basic Energy Sciences, Division of Materials Sciences and Engineering under Award #DE-FG02-96ER45579.

■ REFERENCES

- (1) Hwang, J. Y.; Myung, S. T.; Sun, Y. K. Recent Progress in Rechargeable Potassium Batteries. *Adv. Funct. Mater.* **2018**, *28*, 1802938.
- (2) Pramudita, J. C.; Sehwat, D.; Goonetilleke, D.; Sharma, N. An Initial Review of the Status of Electrode Materials for Potassium-Ion Batteries. *Adv. Energy Mater.* **2017**, *7*, 1602911.
- (3) Eftekhari, A.; Jian, Z.; Ji, X. Potassium Secondary Batteries. *ACS Appl. Mater. Interfaces* **2017**, *9*, 4404–4419.
- (4) Muñoz-Márquez, M. A.; Saurel, D.; Gómez-Cámer, J. L.; Casas-Cabanas, M.; Castillo-Martínez, E.; Rojo, T. Na-Ion Batteries for Large Scale Applications: A Review on Anode Materials and Solid Electrolyte Interphase Formation. *Adv. Energy Mater.* **2017**, *7*, 1700463.
- (5) Wu, X.; Leonard, D. P.; Ji, X. Emerging Non-Aqueous Potassium-Ion Batteries: Challenges and Opportunities. *Chem. Mater.* **2017**, *29*, 5031–5042.
- (6) Liu, J.; Wang, S.; Sun, Q. All-Carbon-based Porous Topological Semimetal for Li-Ion Battery Anode Material. *Proc. Natl. Acad. Sci. U. S. A.* **2017**, *114*, 651–656.
- (7) Liu, J.; Wang, S.; Qie, Y.; Zhang, C.; Sun, Q. High-Pressure-Assisted Design of Porous Topological Semimetal Carbon for Li-Ion Battery Anode with High-Rate Performance. *Phys. Rev. Mater.* **2018**, *2*, No. 025403.
- (8) Xie, H.; Qie, Y.; Imran, M.; Sun, Q. Topological Semimetal Porous Carbon as a High-Performance Anode for Li-Ion Batteries. *J. Mater. Chem. A* **2019**, *7*, 14253–14259.
- (9) Liu, J.; Li, X.; Wang, Q.; Kawazoe, Y.; Jena, P. A New 3D Dirac Nodal-Line Semi-metallic Graphene Monolith for Lithium Ion Battery Anode Materials. *J. Mater. Chem. A* **2018**, *6*, 13816–13824.
- (10) Qie, Y.; Liu, J.; Wang, S.; Sun, Q.; Jena, P. Tetragonal C_{24} : A Topological Nodal-Surface Semimetal with Potential as an Anode Material for Sodium Ion Batteries. *J. Mater. Chem. A* **2019**, *7*, 5733–5739.
- (11) Jiang, X.; Zhao, J.; Li, Y.-L.; Ahuja, R. Tunable Assembly of sp^3 Cross-Linked 3D Graphene Monoliths: A First-Principles Prediction. *Adv. Funct. Mater.* **2013**, *23*, 5846–5853.
- (12) Lv, W.; Zhang, C.; Li, Z.; Yang, Q.-H. Self-Assembled 3D Graphene Monolith from Solution. *J. Phys. Chem. Lett.* **2015**, *6*, 658–668.
- (13) Ben, T.; Ren, H.; Ma, S.; Cao, D.; Lan, J.; Jing, X.; Wang, W.; Xu, J.; Deng, F.; Simmons, J. M.; Qiu, S.; Zhu, G. Targeted Synthesis of a Porous Aromatic Framework with High Stability and Exceptionally High Surface Area. *Angew. Chem.* **2009**, *121*, 9621–9624.
- (14) Kresse, G.; Furthmüller, J. Efficient Iterative Schemes for *Ab Initio* Total-Energy Calculations Using a Plane-Wave Basis Set. *Phys. Rev. B: Condens. Matter Mater. Phys.* **1996**, *54*, 11169–11186.

- (15) Perdew, J. P.; Burke, K.; Ernzerhof, M. Generalized Gradient Approximation Made Simple. *Phys. Rev. Lett.* **1996**, *77*, 3865–3868.
- (16) Heyd, J.; Scuseria, G. E.; Ernzerhof, M. Hybrid Functionals Based on a Screened Coulomb Potential. *J. Chem. Phys.* **2003**, *118*, 8207–8215.
- (17) Blöchl, P. E. Projector Augmented-Wave Method. *Phys. Rev. B: Condens. Matter Mater. Phys.* **1994**, *50*, 17953.
- (18) Monkhorst, H. J.; Pack, J. D. Special Points for Brillouin-Zone Integrations. *Phys. Rev. B* **1976**, *13*, 5188–5192.
- (19) Nosé, S. A Unified Formulation of the Constant Temperature Molecular Dynamics Methods. *J. Chem. Phys.* **1984**, *81*, 511–519.
- (20) Togo, A.; Oba, F.; Tanaka, I. First-Principles Calculations of the Ferroelastic Transition between Rutile-Type and CaCl_2 -Type SiO_2 at High Pressures. *Phys. Rev. B: Condens. Matter Mater. Phys.* **2008**, *78*, 134106.
- (21) Sancho, M. P. L.; Sancho, J. M. L.; Sancho, J. M. L.; Rubio, J. Highly Convergent Schemes for the Calculation of Bulk and Surface Green Functions. *J. Phys. F: Met. Phys.* **1985**, *15*, 851–858.
- (22) Wu, Q.; Zhang, S.; Song, H.-F.; Troyer, M.; Soluyanov, A. A. WannierTools An Open-Source Software Package for Novel Topological Materials. *Comput. Phys. Commun.* **2018**, *224*, 405–416.
- (23) Mills, G.; Jónsson, H. Quantum and Thermal Effects in H_2 Dissociative Adsorption: Evaluation of Free Energy Barriers in Multidimensional Quantum Systems. *Phys. Rev. Lett.* **1994**, *72*, 1124.
- (24) Grimme, S. Semiempirical GGA-Type Density Functional Constructed with a Long-Range Dispersion Correction. *J. Comput. Chem.* **2006**, *27*, 1787–1799.
- (25) Zhang, S.; Wang, Q.; Chen, X.; Jena, P. Stable Three-Dimensional Metallic Carbon with Interlocking Hexagons. *Proc. Natl. Acad. Sci. U. S. A.* **2013**, *110*, 18809–18813.
- (26) Merz, K. M., Jr.; Hoffmann, R.; Balaban, A. T. 3,4-Connected Carbon Nets: Through-Space and through-Bond Interactions in the Solid State. *J. Am. Chem. Soc.* **1987**, *109*, 6742–6751.
- (27) Bucknum, M. J.; Hoffmann, R. A Hypothetical Dense 3,4-Connected Carbon Net and Related B_2C and CN_2 Nets Built from 1,4-Cyclohexadienoid Units. *J. Am. Chem. Soc.* **1994**, *116*, 11456–11464.
- (28) Hoffmann, R.; Kabanov, A. A.; Golov, A. A.; Proserpio, D. M. Homo Citans and Carbon Allotropes: For an Ethics of Citation. *Angew. Chem., Int. Ed.* **2016**, *55*, 10962–10976.
- (29) Umamoto, K.; Wentzcovitch, R. M.; Saito, S.; Miyake, T. Body-Centered Tetragonal C_4 : A Viable sp^3 Carbon Allotrope. *Phys. Rev. Lett.* **2010**, *104*, 125504.
- (30) Chen, Y.; Xie, Y.; Yang, S. A.; Pan, H.; Zhang, F.; Cohen, M. L.; Zhang, S. Nanostructured Carbon Allotropes with Weyl-like Loops and Points. *Nano Lett.* **2015**, *15*, 6974–6978.
- (31) Wang, J.-T.; Weng, H.; Nie, S.; Fang, Z.; Kawazoe, Y.; Chen, C. Body-Centered Orthorhombic C_{16} : A Novel Topological Node-Line Semimetal. *Phys. Rev. Lett.* **2016**, *116*, 195501.
- (32) Liu, J.; Zhao, T.; Zhang, S.; Wang, Q. A New Metallic Carbon Allotrope with High Stability and Potential for Lithium Ion Battery Anode Material. *Nano Energy* **2017**, *38*, 263–270.
- (33) Wu, Z.-j.; Zhao, E.-j.; Xiang, H.-p.; Hao, X.-f.; Liu, X.-j.; Meng, J. Crystal Structures and Elastic Properties of Superhard IrN_2 and IrN_3 from First Principles. *Phys. Rev. B: Condens. Matter Mater. Phys.* **2007**, *76*, No. 054115.
- (34) Tian, Y.; Hu, Z.; Yang, Y.; Wang, X.; Chen, X.; Xu, H.; Wu, Q.; Ji, W.; Chen, Y. In Situ TA-MS Study of the Six-Membered-Ring-Based Growth of Carbon Nanotubes with Benzene Precursor. *J. Am. Chem. Soc.* **2004**, *126*, 1180–1183.
- (35) Krainyukova, N. V.; Zubarev, E. N. Carbon Honeycomb High Capacity Storage for Gaseous and Liquid Species. *Phys. Rev. Lett.* **2016**, *116*, No. 055501.
- (36) Sheng, X.-L.; Yan, Q.-B.; Ye, F.; Zheng, Q.-R.; Su, G. T-Carbon: A Novel Carbon Allotrope. *Phys. Rev. Lett.* **2011**, *106*, 155703.
- (37) Zhang, J.; Wang, R.; Zhu, X.; Pan, A.; Han, C.; Li, X.; Dan, Z.; Ma, C.; Wang, W.; Su, H.; Niu, C. Pseudo-Topotactic Conversion of Carbon Nanotubes to T-carbon Nanowires under Picosecond Laser Irradiation in Methanol. *Nat. Commun.* **2017**, *8*, 683.
- (38) Pang, Z.; Gu, X.; Wei, Y.; Yang, R.; Dresselhaus, M. S. Bottom-Up Design of Three-Dimensional Carbon-Honeycomb with Superb Specific Strength and High Thermal Conductivity. *Nano Lett.* **2017**, *17*, 179–185.
- (39) Zhang, Y.; Sun, H.; Chen, C. Superhard Cubic BC_2N Compared to Diamond. *Phys. Rev. Lett.* **2004**, *93*, 195504.
- (40) Bu, H.; Zhao, M.; Dong, W.; Lu, S.; Wang, X. A Metallic Carbon Allotrope with Superhardness: A First-Principles Prediction. *J. Mater. Chem. C* **2014**, *2*, 2751–2757.
- (41) Tang, W.; Sanville, E.; Henkelman, G. A Grid-based Bader Analysis Algorithm without Lattice Bias. *J. Phys.: Condens. Matter* **2009**, *21*, No. 084204.
- (42) Xu, Z.; Lv, X.; Chen, J.; Jiang, L.; Lai, Y.; Li, J. Dispersion-Corrected DFT Investigation on Defect Chemistry and Potassium Migration in Potassium-Graphite Intercalation Compounds for Potassium Ion Batteries Anode Materials. *Carbon* **2016**, *107*, 885–894.
- (43) Kishore, B.; G, V.; Munichandraiah, N. $\text{K}_2\text{Ti}_4\text{O}_9$: A Promising Anode Material for Potassium Ion Batteries. *J. Electrochem. Soc.* **2016**, *163*, A2551–A2554.
- (44) Dong, Y.; Wu, Z.-S.; Zheng, S.; Wang, X.; Qin, J.; Wang, S.; Shi, X.; Bao, X. Ti_3C_2 MXene-Derived Sodium/Potassium Titanate Nanoribbons for High-Performance Sodium/Potassium Ion Batteries with Enhanced Capacities. *ACS Nano* **2017**, *11*, 4792–4800.
- (45) Han, J.; Xu, M.; Niu, Y.; Li, G.-N.; Wang, M.; Zhang, Y.; Jia, M.; Li, C. m. Exploration of $\text{K}_2\text{Ti}_8\text{O}_{17}$ as an Anode Material for Potassium-Ion Batteries. *Chem. Commun.* **2016**, *52*, 11274–11276.
- (46) Aydinol, M.; Kohan, A.; Ceder, G.; Cho, K.; Joannopoulos, J. Ab Initio Study of Lithium Intercalation in Metal Oxides and Metal Dichalcogenides. *Phys. Rev. B: Condens. Matter Mater. Phys.* **1997**, *56*, 1354.